HEALTH AND MEDICINE

Wireless, implantable catheter-type oximeter designed for cardiac oxygen saturation

Wei Lu[1]*, Wubin Bai[2,3]*, Hao Zhang[2,4]*, Chenkai Xu[5], Antonio M. Chiarelli[6], Abraham Vázquez-Guardado[1], Zhaoqian Xie[7], Haixu Shen[2], Khizar Nandoliya[8,9], Hangbo Zhao[1,10], KunHyuck Lee[11], Yixin Wu[2], Daniel Franklin[1,2], Raudel Avila[11], Shuai Xu[1,12], Alina Rwei[1,13], Mengdi Han[1], Kyeongha Kwon[1,14], Yujun Deng[11,15,16], Xinge Yu[17], Edward B. Thorp[18], Xue Feng[19], Yonggang Huang[1,2,11,15], Joseph Forbess[20,21], Zhi-Dong Ge[18,21†], John A. Rogers[1,2,5,8,9,11,22†]

Accurate, real-time monitoring of intravascular oxygen levels is important in tracking the cardiopulmonary health of patients after cardiothoracic surgery. Existing technologies use intravascular placement of glass fiber-optic catheters that pose risks of blood vessel damage, thrombosis, and infection. In addition, physical tethers to power supply systems and data acquisition hardware limit freedom of movement and add clutter to the intensive care unit. This report introduces a wireless, miniaturized, implantable optoelectronic catheter system incorporating optical components on the probe, encapsulated by soft biocompatible materials, as alternative technology that avoids these disadvantages. The absence of physical tethers and the flexible, biocompatible construction of the probe represent key defining features, resulting in a high-performance, patient-friendly implantable oximeter that can monitor localized tissue oxygenation, heart rate, and respiratory activity with wireless, real-time, continuous operation. In vitro and in vivo testing shows that this platform offers measurement accuracy and precision equivalent to those of existing clinical standards.

INTRODUCTION

The cardiovascular system delivers oxygen and nutrients to tissues and cells in the body (*1*). Maintaining an adequate balance between oxygen delivery and consumption is essential for cellular physiological function (*2*). Accurate and real-time monitoring of specific intracardiac and major vascular oxygen saturations after open-heart surgery is critically important for treating patients, especially those who suffer from cyanotic congenital heart defects. Widely used wearable oximeters (*3*) and the clinical pulse oximeters (*4*) capture global oxygenation of the body. These measurements do not contain information on localized tissue oximetry (*5*), either the intracardiac or intravascular oxygen saturation. The measurement of these saturations is performed during diagnostic cardiac catheterization to calculate cardiac output and derive vascular resistances. In the intensive care unit (ICU) setting, the intravenous fiber-optic oximetric catheter is used to monitor continuously blood oxygen saturation (*6*, *7*), obtained either as mixed venous oxygen saturation (SvO_2, a reflection of the global balance between oxygen delivery and consumption as it is measured in the pulmonary artery) or as central venous oxygen saturation ($ScvO_2$, a reflection of regional oxygen extraction from the brain and the upper part of the body as it is measured from a central vein) (*1*, *2*, *8*, *9*).

Existing fiber-optic catheter oximeters use hard glass fiber waveguides to deliver light from an external source to the blood at the tip of the catheter and to transmit some fractions of the backscattered light back to an external unit for detection (*10*). Here, the fiber-optic catheter connects to a light source and sensing module (*11*), and an additional interface joins the system to an apparatus that contains processing and driving circuits, display monitor, and controlling software (*12*). The complete system provides an effective tool for monitoring venous oxygenation via insertion of the catheter probe through a vein to a desired location, but it tethers the patient to bedside hardware, thereby limiting their freedom of movement and complicating the simultaneous use of other diagnostic or therapeutic

[1]Center for Bio-Integrated Electronics, Northwestern University, Evanston, IL 60208, USA. [2]Department of Materials Science and Engineering, McCormick School of Engineering, Northwestern University, Evanston, IL 60208, USA. [3]Department of Applied Physical Sciences, University of North Carolina at Chapel Hill, Chapel Hill, NC 27514, USA. [4]Department of Chemistry, Key Laboratory of Bioorganic Phosphorus Chemistry and Chemical Biology, Tsinghua University, Beijing, China. [5]Department of Biomedical Engineering, McCormick School of Engineering, Northwestern University, Evanston, IL 60208, USA. [6]Institute of Advanced Biomedical Technologies and Department of Neuroscience, Imaging and Clinical Sciences, University G. D'Annunzio of Chieti–Pescara, Chieti 66100, Italy. [7]State Key Laboratory of Structural Analysis for Industrial Equipment, Department of Engineering Mechanics, International Research Center for Computational Mechanics, Dalian University of Technology, Dalian 116024, China. [8]Department of Chemistry, McCormick School of Engineering, Northwestern University, Evanston, IL 60208, USA. [9]Department of Neurological Surgery, Feinberg School of Medicine, Northwestern University, Chicago, IL 60611, USA. [10]Department of Aerospace and Mechanical Engineering, University of Southern California, Los Angeles, CA 90089, USA. [11]Department of Mechanical Engineering, Northwestern University, Evanston, IL 60208, USA. [12]Department of Dermatology, Feinberg School of Medicine, Northwestern University, Chicago, IL 60611, USA. [13]Department of Chemical Engineering, Delft University of Technology, Delft, Netherlands. [14]School of Electrical Engineering, Korea Advanced Institute of Science and Technology, Daejeon 34141, Republic of Korea. [15]Department of Civil and Environmental Engineering, Northwestern University, Evanston, IL 60208, USA. [16]State Key Laboratory of Mechanical System and Vibration, Shanghai Jiao Tong University, Shanghai 200240, China. [17]Department of Biomedical Engineering, City University of Hong Kong, Kowloong Tong, Hong Kong. [18]Department of Pathology, Feinberg School of Medicine, Northwestern University, 300 E. Superior Avenue, Chicago, IL 60611, USA. [19]AML, Department of Engineering Mechanics Center for Flexible Electronics Technology, Tsinghua University, Beijing 100084, China. [20]Children's Heart Program, Division of Cardiac Surgery, Department of Surgery, University of Maryland School of Medicine 110 S. Paca Street Baltimore, MD 21201, USA. [21]Division of Cardiovascular-Thoracic Surgery, Departments of Surgery and Pediatrics, Ann & Robert H. Lurie Children's Hospital of Chicago; Feinberg School of Medicine, Northwestern University, 225 E. Chicago Avenue, Chicago, IL 60611, USA. [22]Departments of Electrical Engineering and Computer Science, McCormick School of Engineering, Northwestern University, Evanston, IL 60208, USA.
*These authors contributed equally to this work.
†Corresponding author. Email: zhi-dong.ge@northwestern.edu (Z.-D.G.); jrogers@northwestern.edu (J.A.R.)

tools. Moreover, the rigid properties of the glass fiber can induce adverse events during long-term implantation, e.g., damage to blood vessels, infection, or thrombosis (*13*–*17*). For all patients who receive catheters, mechanical complications are reported to occur in 5 to 19% of patients, infectious complications in 5 to 26%, and thrombotic complications in 2 to 26% (*13*). Alternative approaches based on biomaterial waveguides, sometimes bioresorbable materials, have some utility but suffer from disadvantages in transmission losses, coupling losses, and time-dependent effects associated with bending and other motion-related artifacts (*18*, *19*). In addition, these platforms can induce similar adverse complications as with conventional fiber-optic catheters. Such complications are particularly frequent and severe in infants and children. An unmet clinical need is in an alternative type of oximeter designed to provide real-time, accurate intravascular oxygen saturation yet avoid adverse effects that can occur in these and other high-risk patients.

Recent advances in soft, wireless electronics (*20*–*24*) and in associated technologies for wireless localized tissue oximetry (*25*) and wearable oximetry (*3*, *20*) provide the foundations for designing unique platforms that overcome these challenges in cardiovascular monitoring. The platform introduced here consists of a thin, flexible catheter-type optoelectronic probe that connects to a small, wearable electronic module for wireless, real-time, and continuous measurements of intravascular oxygen saturation with clinical-grade accuracy. The probe tip in this case includes high-performance, miniaturized light-emitting diodes (LEDs) and photodiode (PD), fully encapsulated with medical-grade, soft, transparent silicone elastomer. The electronic module supports rechargeable powering, circuit control, signal processing, and wireless data communication based on Bluetooth protocols. A graphical user interface (GUI) deployed on a smartphone or tablet computer or ICU monitoring display enables real-time visualization, storage, and analysis of measurement data. The absence of physical tethers, the soft, biocompatible construction of the probe, and the lateral (as opposed to distal) configuration of the measurement represent key defining features.

Systematic studies of these systems inform optimized choices for the materials, the mechanical layouts, the thermal management approaches, the encapsulation strategies, and the optical setups. Tests on healthy human volunteers yield data that are in excellent agreement with clinical standard pulse oximeters for global oxygen saturation and heart rate (HR) measurement. Investigations using rat models show that the catheter can be implanted and sutured to the cardiac surface and that the measured oximetry values match those determined using a clinical blood gas analyzer. These results represent potentially important advances in wireless optoelectronic technologies for cardiovascular care.

RESULTS

Design features

Figure 1A illustrates the operational characteristics of an implantable, wireless catheter-type optoelectronics system, highlighting its miniaturized, biocompatible design and capabilities for wireless [Bluetooth low energy (BLE)], real-time monitoring at the surface of the heart. The integrated platform, fully encapsulated with a medical-grade silicone layer, consists of three main components: (i) a low-modulus, flexible catheter with an optoelectronic sensor that contains two light-emitting diodes with emission wavelengths of 645 and 950 nm, respectively, and one silicon PD; (ii) a bendable, miniaturized, battery-powered BLE electronic module that can gently mount onto the skin; and (iii) a custom GUI deployed on a handheld device that supports real-time visualization, storage, and analysis of measurement data and provides a control interface for setting the illumination parameters for the LEDs (Fig. 1A). In the use case considered here, the sensing probe can be placed on the surface of the desired cardiovascular structure, where it is mechanically stabilized with fine sutures. Electrical interconnects attach to the BLE module, secured with a skin-safe adhesive onto the chest.

The exploded view schematic illustration of this module (Fig. 1B) highlights an elastomeric substrate (Silbione RTV 4420, Elkem), a flexible printed circuit board (fPCB) with a collection of electronic components, a rechargeable lithium-ion battery, and a top encapsulation layer (Silbione RTV 4420, Elkem). Figure 1C presents a magnified view of the probe, with its two LEDs and PD, and two opaque silicone-based cuboid structures [polydimethylsiloxane (PDMS) mixed with 5% of Silc-Pig silicone opaque dye; $L \times W \times H$: 1 mm × 0.5 mm × 0.8 mm] for light blocking, all mounted on an fPCB in the geometry of a narrow, thin strip (width, 1.3 mm; thickness, 111 μm; length, 14 mm), which connects, through thin, Teflon-coated copper wires (diameter, 80 μm), to the BLE module. A small plug-in connector serves as an electrical interface between the probe and the module and allows battery recharge using a wired interface. A medical-grade, biocompatible silicone (MED-1000, Avantor Inc.) fully encapsulates the optical sensing probe to define a cylindrical shape (diameter, 1.5 mm) and smooth surface that facilitates surgical manipulation and insertion. The light-blocking elements lie between the PD and LEDs and at the probe tip close to the other sides of the LEDs to eliminate parasitic transmission of light from the LEDs directly to the PD without passing through the surrounding tissue of interest. The distance between the LEDs and the PD sets the characteristic depth associated with the detected backscattered light (*25*, *26*). Increasing this distance enlarges the effective probing volume and enhances the changes in signal associated with changes in blood oxygenation but also decreases the amount of light detected by the PD due to increased absorption and scattering events in the light path (*3*, *27*). The geometry reported here positions the PD equidistant between the two LEDs, at a distance of 2 mm, selected to balance sensing depth, probing volume, and signal-to-noise ratio.

Figure 1D presents an image of a device wrapped onto a glass rod with radius around 1 cm to highlight its flexibility. Figure 1 (E and F) shows top-down views of the layout of the electronic components, with a corresponding schematic block diagram in Fig. 1G. The red and near-infrared (NIR) LEDs at the tip end of the probe receive power from driving circuitry modulated by a microcontroller unit (MCU) in the BLE module such that the LEDs turn off and on out of phase. The PD output passes through a transimpedance amplifier to yield an amplified voltage signal. A 14-bit analog-digital converter (ADC) supports signal sampling at a rate of 200 samples per second (Sa/s), corresponding to 100 Sa/s for each LED. The MCU performs smoothing on the raw data with a finite impulse response seven-point moving average filter, as a low-pass filter with a cutoff frequency of 6.4 Hz at a sampling speed of 100 Sa/s. Data transfer occurs wirelessly to a personal computer through BLE protocols. A custom GUI software serves as a control interface and mechanism for data storage and display. Established data analytics routines yield HR and oximetry values, as described in Materials and Methods.

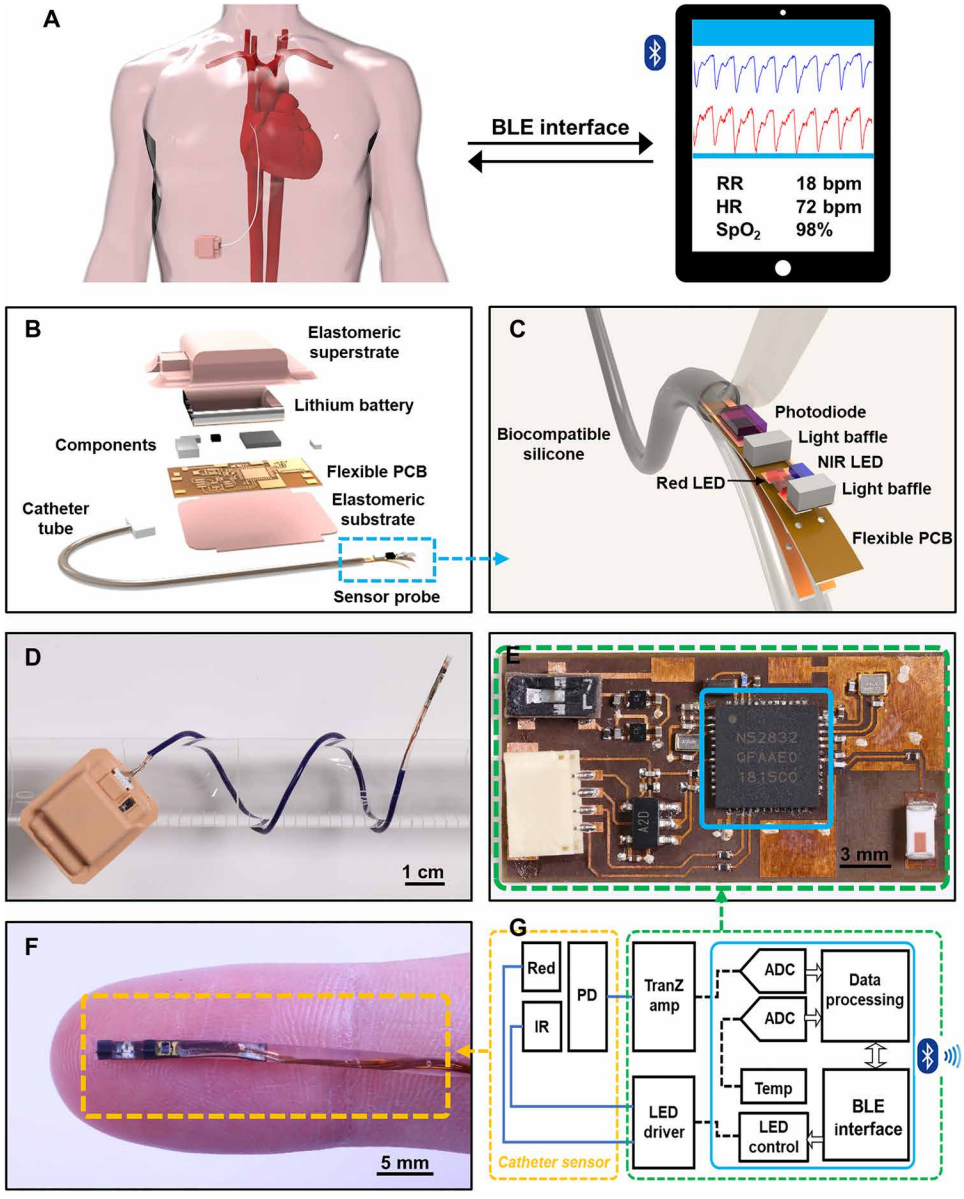

Fig. 1. Implantable, wireless catheter oximeter for real-time monitoring of cardiac physiology in the context of surgical procedures. (**A**) Schematic illustration of the use of an implanted device for wireless blood oximetry near the cardiac surface. The system consists of a catheter-type oximeter with sensing tip sutured onto the surface of the heart, interfaced to an electronic module that attaches to the skin for signal collection and wireless data transmission through Bluetooth protocols. A custom GUI displays and records the data on a computer and serves as a control interface to the device. (**B** and **C**) Exploded view schematic illustration of the device design. (B) The electronic module contains five layers: a bottom elastomeric substrate, a flexible PCB, a collection of electronic components, a lithium ion battery, and a top elastomeric encapsulation. (C) The enlarged image shows the sensor probe, which consists of a flexible PCB, optical stimulation and sensing components, and optical blocking modules. The probe has a diameter of 1.5 mm and is fully encapsulated with transparent, biocompatible silicone. (**D**) Image of a catheter oximeter wrapped around a glass rod. (**E**) Image of an electronic module without encapsulation. (**F**) Image of a catheter-type oximetry sensor. (**G**) Schematic block diagram of the system. Photo credit: Wei Lu and Wubin Bai, Northwestern University.

Optical, thermal, and electrical characterization

Oxyhemoglobin (HbO_2) and deoxyhemoglobin (Hb) correspond to hemoglobin with and without bound oxygen, respectively. Well-known optical approaches provide effective estimates of blood oxygen saturation, defined as the fraction of HbO_2 relative to total hemoglobin (HbO_2 + Hb) (*4*, *28*), by comparing the distinct absorption spectra of HbO_2 and Hb in the visible and NIR spectral range. Figure 2A shows the measured emission spectral profiles of the red and NIR LEDs and their peak emission wavelengths at 645 nm and 950 nm, respectively, along with the molar extinction coefficient (ε) spectra of HbO_2 and Hb (*29*). The data show an isosbestic point near 800 nm, where Hb and HbO_2 have the same ε. For wavelengths above and below, the values of ε for HbO_2 and Hb change in relative magnitude. The large differences at 645 and 950 nm establish the basis of optical measurements of blood oxygenation based on the Beer-Lambert law.

The probe uses a single high-speed PD (TEMD7000X01, Vishay Semiconductors Inc.) with relative spectral sensitivities S(λ) at 950 and 640 nm of 99 and 54%, respectively (fig. S2A) (*30*). Figure

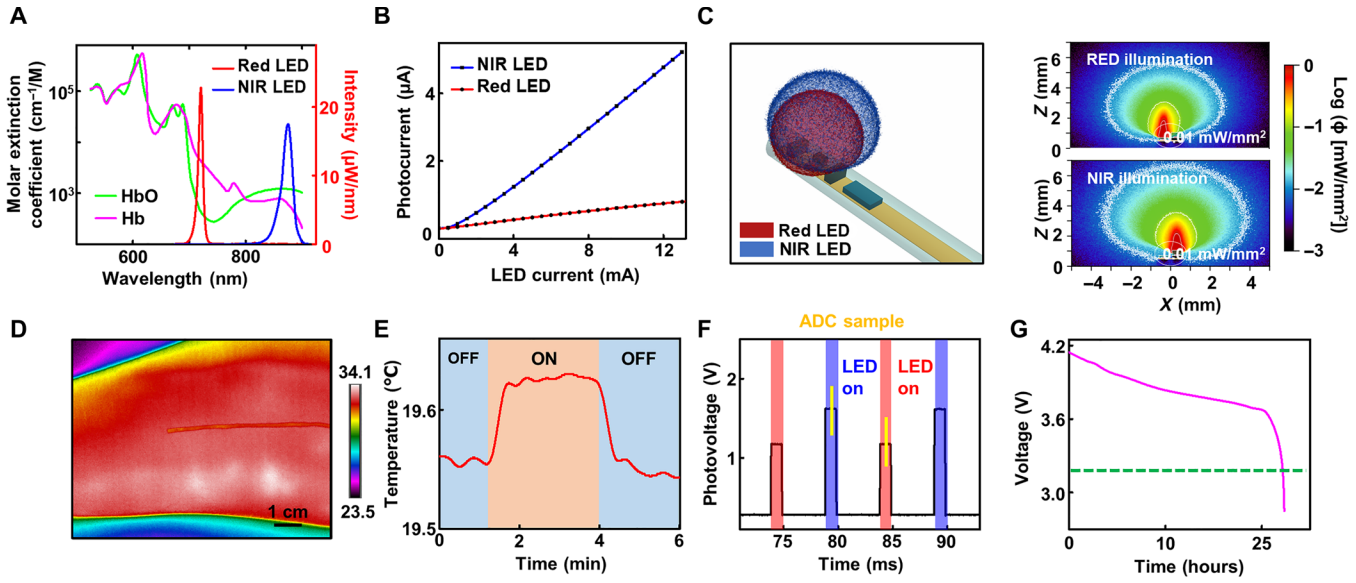

Fig. 2. Optical, thermal, and electronic characteristics. (**A**) Spectral properties of light emission from the red and NIR LEDs used for the sensor probe. These LEDs (peak wavelengths of 645 and 950 nm) cover the parts of the spectrum of reversed absorption properties for Hb and HbO_2. (**B**) Measured photocurrent as a function of input current for red and NIR LEDs, with the sensor probe implanted into raw meat. The experimental setup appears in fig. S3. (**C**) Monte Carlo simulation of the spatial distribution of normalized emission intensity profiles from the NIR and red LEDs in cardiac tissue. (**D**) Thermal image showing the temperature distribution of the skin of an adult arm with a catheter probe placed on top. (**E**) Measured temperature of the oximeter sensor probe during operation, with activation at 1 min and deactivation at 4 min. The sensor induces minimal increase in temperature (less than 0.08°C). (**F**) Measured photovoltage output from the amplifier circuit as a function of time during a driving clock sequence of red and NIR LEDs and ADC sampling. Narrowing the driving pulses for the LEDs effectively reduces the power consumption and prolongs battery lifetime. (**G**) Battery voltage as a function of working time. A 45-mAh lithium battery supports operation for at least 22 hours.

S2B illustrates the photocurrent response to illumination with light passed through a chopper (red light, wavelength: 633 nm). The results suggest response times less than 1 ms, sufficient for current purposes. Figure 2B shows the photocurrent from the red and NIR LEDs with the probe buried inside muscle tissue collected from a bovine model (fig. S3A). The red light induces lower photocurrent response compared to the NIR by a factor of ~6.5 for the same drive current, consistent with differences in the efficiencies of the two LEDs and in the spectral response of the PD. The PD exhibits a linear response with illumination intensity at both wavelengths. Based on these observations and on power and circuit considerations, the devices use drive currents of 3.1 mA (9.2 mW/mm^2) and 1.8 mA (14.4 mW/mm^2) for the red and NIR LEDs, respectively, thereby generating corresponding photocurrents with a ratio of 1:2.3.

The physics of light transport in biological tissues can be captured numerically using the Monte Carlo method (*31*). The results provide quantitative insights into the illumination distributions around the LEDs and into aspects of light detection by the PD (Fig. 2C). The model uses the optical properties of human cardiac muscle tissue found in the literature (*32*). Other details of the simulation appear in Materials and Methods. Figure 2C shows normalized emission intensity profiles of the red and NIR LEDs as a function of distance, in three dimensions (left) and in two dimensions at a cross-sectional plane across the LEDs (right). The penetration depth, where the optical irradiance decreases to 0.01 mW/mm^2, is 3.84 and 5.16 mm for the red and NIR LEDs, respectively. The illumination volume is 85.3 and 159.8 mm^3, respectively, for red and NIR LEDs (fig. S4, A and B). Moreover, by varying the intensity from 0 to 50 mW/mm^2 (fig. S4, C and D), the penetration depth varies from 0 to 7 mm, with an illumination volume up to 600 mm^3. This adjustable illumination depth and volume can be useful for different application requirements, from thin tissues associated with blood vessels to thick tissues such as those of the myocardium, to measure either intracardiac or intravascular oxygenation.

Thermal images (Fig. 2D) collected with an IR camera (FLIR A325SC, FLIR Systems) show no apparent increase in temperature around the LEDs during operation of a device pressed against the skin. Driving the LEDs and sampling the PD response at low duty cycles (10% duty cycle with 1-ms pulse widths at 100-Hz sampling rate, as shown in Fig. 2F) leads to low power consumption and low heat generation while preserving well-defined modulation, as shown for the case of the probe placed at the fingertip (Fig. 4C). A small-scale negative temperature coefficient (NTC) thermistor allows quantitative evaluation of the temperature near a probe inserted into pieces of raw meat (fig. S3B). The measurements indicate a small increase in temperature (~0.08°C) during operation of the device (Fig. 2E), consistent with the results of finite element analysis (FEA) in which the average temperature rise of four points around the active LEDs in the probe is roughly 0.1°C, as shown in fig. S5. Although this increase is higher than that expected for conventional fiber-optic catheter oximeters, it is more than 30 times lower than the maximum allowed increase in the temperatures of internal tissues (i.e., 3°C) (*33*, *34*). The measured rise time is comparable to that determined by simulation, i.e., ~20 s (details on this measurement and simulation appear in Materials and Methods).

Minimizing the duty cycle also reduces the power consumption of the system and thereby extends the battery life. The system reported here uses a 45-mAh rechargeable lithium battery. For operational parameters described previously, this battery supports continuous operation and wireless data streaming at 200 Sa/s for more than 22 hours using a 10% duty cycle (Fig. 2G). Reducing the sampling frequency

can further prolong the battery life, depending on requirements. For instance, measurements performed every 5 min, for a duration of 5 s, with the system in sleep mode for other times will extend the battery life by 60 times, corresponding to roughly 1300 hours.

Mechanical characterization and encapsulation performance

The compliant mechanical properties of the device minimize mechanical forces on adjacent biological tissues for improved biocompatibility. Human skin has Young's modulus between ~400 and ~800 kPa (*35*, *36*), while human cardiac muscles have Young's moduli of ~100 kPa (*37*). The BLE module uses a biocompatible silicone (Silbione RTV 4420) for encapsulation, with a modulus in the range of human skin. The catheter oximeter probe uses three different biocompatible silicones (MED-1040, MED-1000, and MED-1037, Avantor Inc.), with Young's modulus values of 797, 1022, and 1667 kPa as in Fig. 3A (measurement data are shown in fig. S6), suitable for different medical applications. Choices of the silicone and the diameter of the copper wire can be selected to achieve bending stiffnesses of 1.6, 1.8, and 2.3 to 20 N/mm^2. By comparison, commercial catheter oximeters for central venous applications use optical fibers

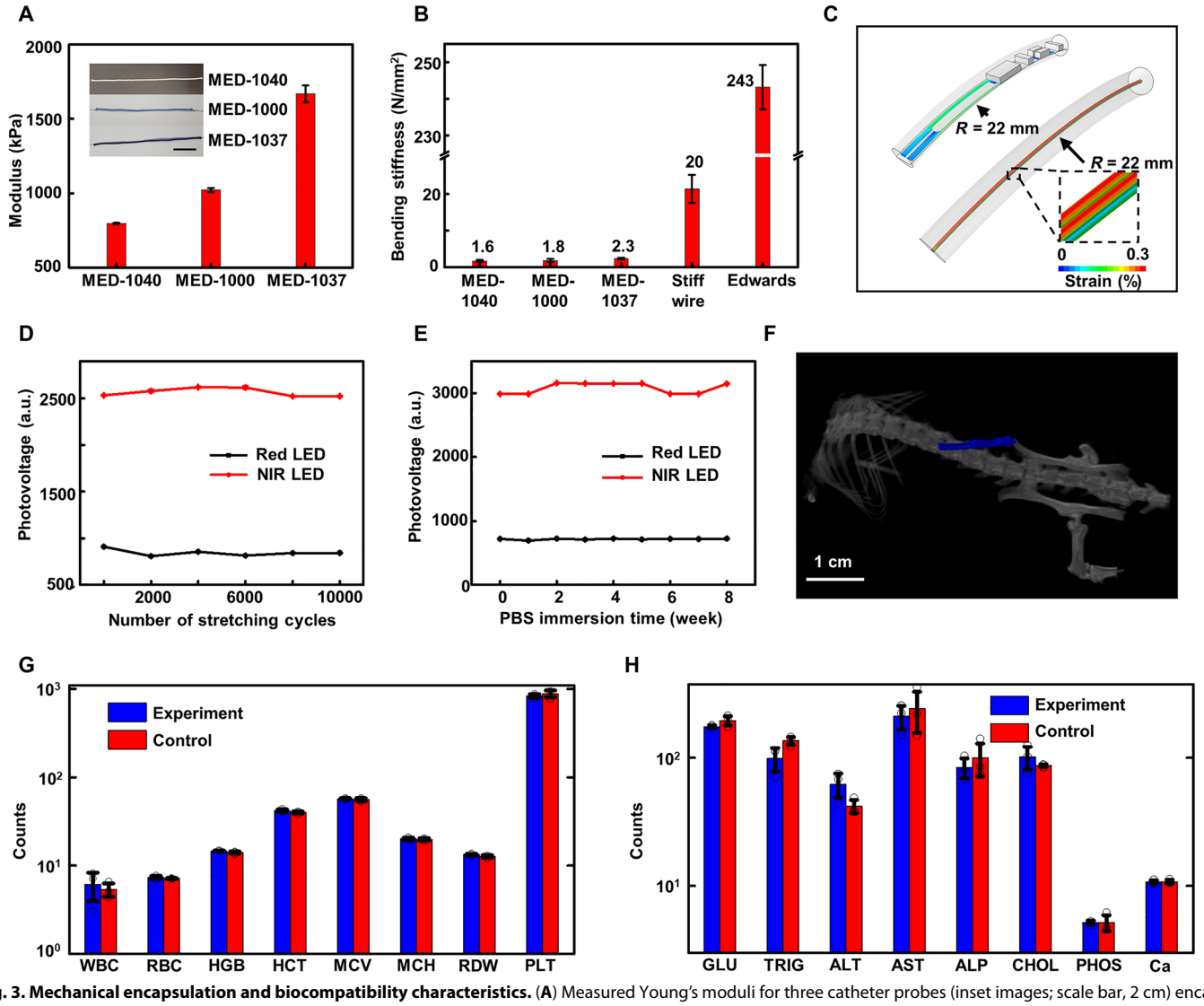

Fig. 3. Mechanical encapsulation and biocompatibility characteristics. (**A**) Measured Young's moduli for three catheter probes (inset images; scale bar, 2 cm) encapsulated with three different biocompatible silicone elastomers (labeled: MED-1040, MED-1000, and MED-1037, respectively). The Young's moduli of the three catheter probes range from 800 to 1700 kPa. (**B**) Measured bending stiffnesses for the three catheter probes in (A), a catheter probe fabricated from relatively stiff copper wire encapsulated with MED-1000, and a commercial fiber-optic catheter (Swan Ganz 777F8, Edwards LifeSciences Inc.). The bending stiffnesses are 1.6, 1.8, 2.3, 20, and 243 N/mm^2, respectively. (**C**) Finite element modeling of the sensor probe and catheter subjected to a bending radius of 22 and 27 mm, respectively. (**D**) Measured photovoltage from the catheter probe as a function of cycles of compression and bending. Experimental details appear in figs. S7 and S8. The photovoltage generated from the photodetector corresponds to operation of the two LEDs (peak wavelengths of 645 and 950 nm, respectively) at the tip of the catheter probe. a.u., arbitrary units. (**E**) Measured photovoltage as a function of immersion time in PBS solution at 37°C. Experimental details appear in figs. S10 and S11. The data indicate negligible change in performance over 8 weeks. (**F**) CT image of the catheter sensor after 2 weeks of implantation. (**G** and **H**) Analysis of complete blood count (G) and blood chemistry (H) for mice with an oximetry probe implanted subcutaneously for 30 days (labeled as Experiment) and for mice without device implantation (labeled as Control). Additional experiment results, abbreviations, and corresponding units are presented in fig. S13.

(e.g., Swan Ganz 777F8, Edwards LifeSciences Inc.) with bending stiffnesses of ~250 N/mm^2 (Fig. 3B), which is 10 to 150 times larger than those of devices reported here. The left ventricle of the adult human cardiac tissue has a typical thickness of 12 to 15 mm (*38*). The resulting bending stiffness is ~50 times larger than that of the probe. The probe can therefore easily and conformally deform with the heart muscle with negligible mechanical load or associated damage to the heart, although the modulus of the probe is higher than that of the cardiac tissue.

Results of FEA in Fig. 3C show that the strain distribution in the copper remains below the elastic strain limit (0.3%) in the sensor probe and silicone-based catheter for a bending radius of 22 and 27 mm, respectively. Studies indicate that bending to radii of 5 mm for more than 10,000 cycles leads to no change in the device performance (fig. S7B). Specifically, Fig. 3D shows consistent photovoltages generated from the PD by operation of the red and NIR LEDs, with additional measurements inside an integrating sphere after various bending cycles (measurement data in fig. S8). Figure S9 shows signals generated from a finger, indicating stable performance over 10,000 bending cycles. The silicone encapsulation also provides an adequate barrier to biofluids. Immersion into a bath of phosphate-buffered saline (PBS) at 37°C for 8 weeks (fig. S10) induces a negligible change in device performance examined by both in vitro measurements inside the integrating sphere (Fig. 3E and fig. S11) and tests on the fingertips (fig. S12). The data of Fig. 3E use the same measurement approach as those in Fig. 3D; fig. S12 uses the methods of fig. S9. All results indicate that the system supports stable performance over 8 weeks of immersion in PBS.

Figure 3F presents a computed tomography (CT) image of a mouse model 2 weeks after subdermal implantation of a device on the back near the spine. Analysis of complete blood count (Fig. 3G) and blood chemistry (Fig. 3H) for mice with implants for 30 days (labeled as Experiment) and mice without implants (labeled as Control) indicates no sign of organ damage or injury and no change in the electrolyte or enzyme balance. More measured parameters are presented in fig. S13 (details appear in Materials and Methods).

Bench tests

SvO_2 and $ScvO_2$ are two essential diagnostic indicators. The former, measured in the pulmonary artery, reflects the global balance between oxygen delivery and consumption. The latter, measured via a central venous catheter, reflects principally the degree of oxygen extraction from the brain and the upper part of the body (*1*, *2*, *8*, *39*). Major surgeries, especially cardiac surgeries, rely on monitoring of SvO_2 and $ScvO_2$ with fiber-optic oximeters (e.g., Swan Ganz series catheter and HemoSphere monitoring platform, Edwards LifeSciences Inc.) to guide care (*6*, *7*). Such devices are implanted transvenously, where the fiber optics support the optical transmission from external sources and sensing of backscattered light using external detectors, thereby tethering the patient to bedside apparatus (*2*, *40*). Figure 3 (A and B) summarizes some advantages of the introduced wireless catheter probe in materials and mechanical properties, compared with a commercially available fiber-optic probe, and Fig. 4 (A and B) offers comparisons of optical performance and sensitivity of these two systems.

Figure 4A (left) shows comparisons based on measurements obtained by placing both the wireless catheter oximetry probe and a commercial fiber-optic oximetry catheter (Swan Ganz 777F8, Edwards LifeSciences Inc.) in a fluorescent solution with 0.3 μM Alexa Fluor 647 (emission maximum at 672 nm when excited at 651 nm). The device introduced here involves a divergent illumination pattern normal to the surface of the LED and lateral to the long axis of the probe. By contrast, the commercial device exhibits a conical pattern of illumination with a low divergence angle centered at the tip of the fiber (Fig. 4A, left). Monte Carlo simulations of the light emission profiles for these two type sensors (Fig. 4A, right) are consistent with experimental results (Fig. 4A, left). The divergent and lateral emission features of the LED system maximize light-tissue coupling for a range of implantation sites, especially those that involve coupling to the surface of the heart. Moreover, the probe volume and probe depth can be adjusted by control over the light intensity (fig. S4) and the distance between the LEDs and PD to allow optimization for measurements of localized tissue oximetry across various length scales, ranging from those relevant for small animals (e.g., rat) to large animals (e.g., swine) and humans. Adjusting the pulse width and duty cycle for operating the LEDs and optimizing the configuration of the light blocking elements (Fig. 1C) in the probe eliminate limitations associated with thermal effects and optical interference.

In vitro tests of the device with horse blood (Fisher Scientific) at various oxygenation levels yield results that agree well with those measured with the commercial system (Fig. 4B), with a correlation coefficient of 0.979. Adding sodium dithionite into the blood effectively transforms oxygenated hemoglobin into the deoxygenated form. The amount of sodium dithionite defines the oxygenation level across a relevant range (measurement and calculated data are shown in figs. S14 and S15, and details on the measurements and calculation methods appear in Materials and Methods). The results demonstrate measurement capabilities for assessments of SvO_2 and $ScvO_2$ across relevant ranges.

A simple demonstration involves measurements of pulse oxygen saturation by pressing the device onto an index finger (fig. S16), as raw pulse signal shown in Fig. 4C. Standard postprocessing algorithms based on the Beer-Lambert law (Fig. 4D) yield the pulse oxygen saturation (SpO_2) and HR (with the algorithms described in detail in Materials and Methods). Figure 4 (E and F) presents results from a subject during a period of rest followed by a breath holding and then another period of rest. The data match well with those determined with a clinical pulse oximeter (DASH 3000 Patient Monitor, General Electronic Inc.) attached onto the other finger. Additional independent experiments on different subjects appear in fig. S17. The Bland-Altman plot in Fig. 4 (G and H) highlights excellent agreement between the wireless catheter oximeter and the clinical gold standard oximeter in measuring pulse oximetry and HR. With a total of 801 data points on four independent subjects, the 95% confidence interval for SpO_2 is [−3.61 to 3.90] and for HR is [−4.05 to 3.85] bpm (breaths per minute).

In vivo studies

The primary envisioned application of the technology introduced here is in the context of pediatric cardiac surgery and recovery, where sutures hold the probe against the surface of major cardiac vessels for real-time monitoring of oxygen saturation within that vessel during the early and critical postoperative period of several days. Experiments on rat models, as illustrated in Fig. 5A, demonstrates the key features. Figure S18 shows some details. The implantation procedures appear in Materials and Methods. Sutures hold the probe to the anterior wall of the left ventricle [with thickness of ~2.6 mm (*41*)] close to the left anterior descending

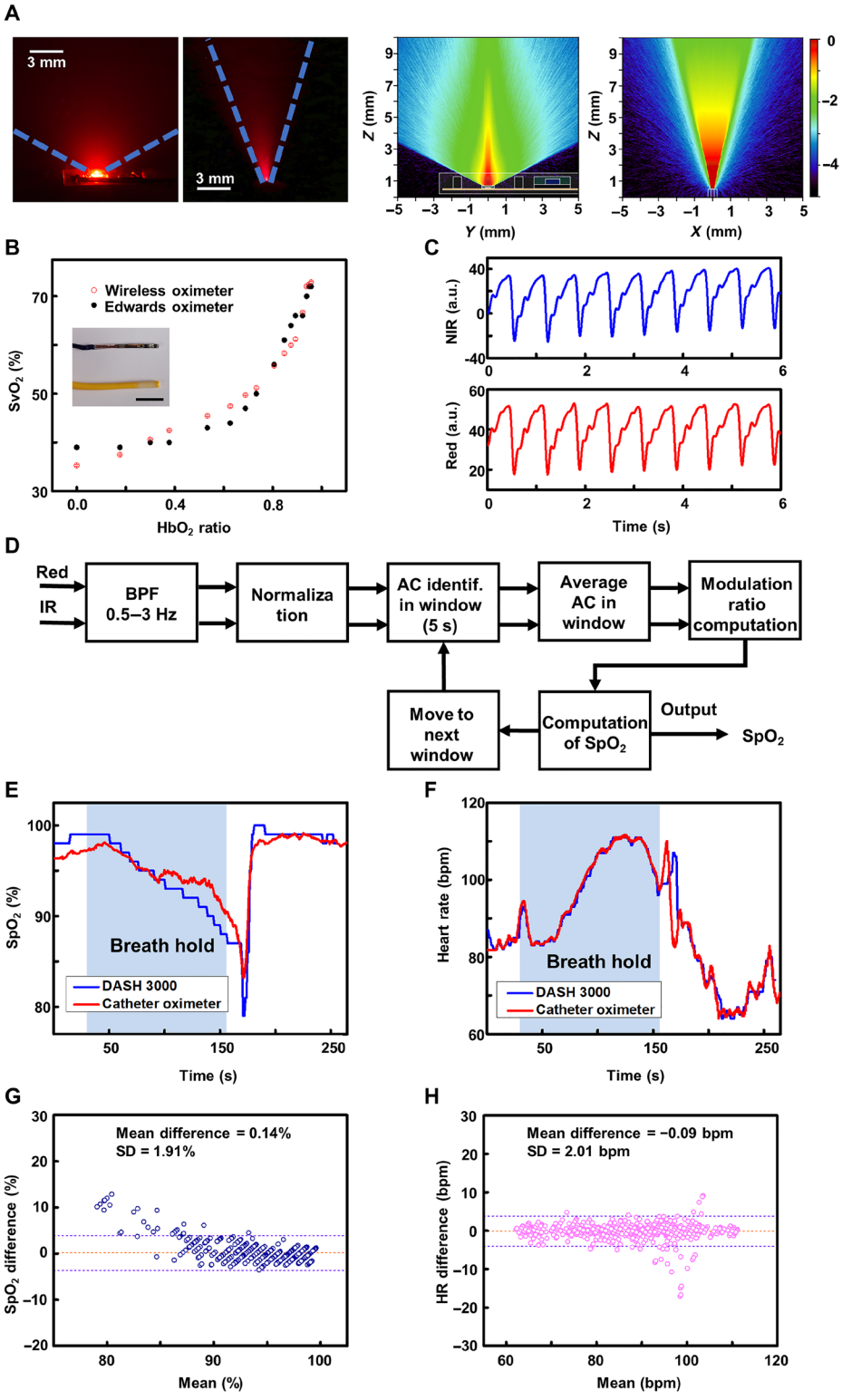

Fig. 4. Performance characteristics for oximetry measurements. (**A**) Comparisons of light emission profiles of a commercial catheter oximeter (Swan Ganz 777F8, Edwards LifeSciences Inc.) and the device introduced here. (**B**) Comparisons of the commercial catheter oximeter and the device introduced here in measuring the oxygen saturation in blood solutions with different ratios of HbO_2 and Hb. The inset image shows a comparison of the wireless catheter probe and a commercial fiber-optic catheter (scale bar, 1 cm). (**C**) Measured pulse signals from the device placed on the index finger of an adult. (**D**) Algorithm flow chart of the calculation of pulse oximetry based on photovoltage signals. (**E** and **F**) Measured SpO_2 (E) and HR (F) during a period of rest followed by a breath hold and then another period of rest. The results match those obtained with a commercial oximeter (General Electronic Inc). The results of additional experiments appear in fig. S17. (**G** and **H**) Bland-Altman plots. (G) SpO_2 from finger (four subjects, 801 points). (H) HR from finger (4 subjects, 801 points).

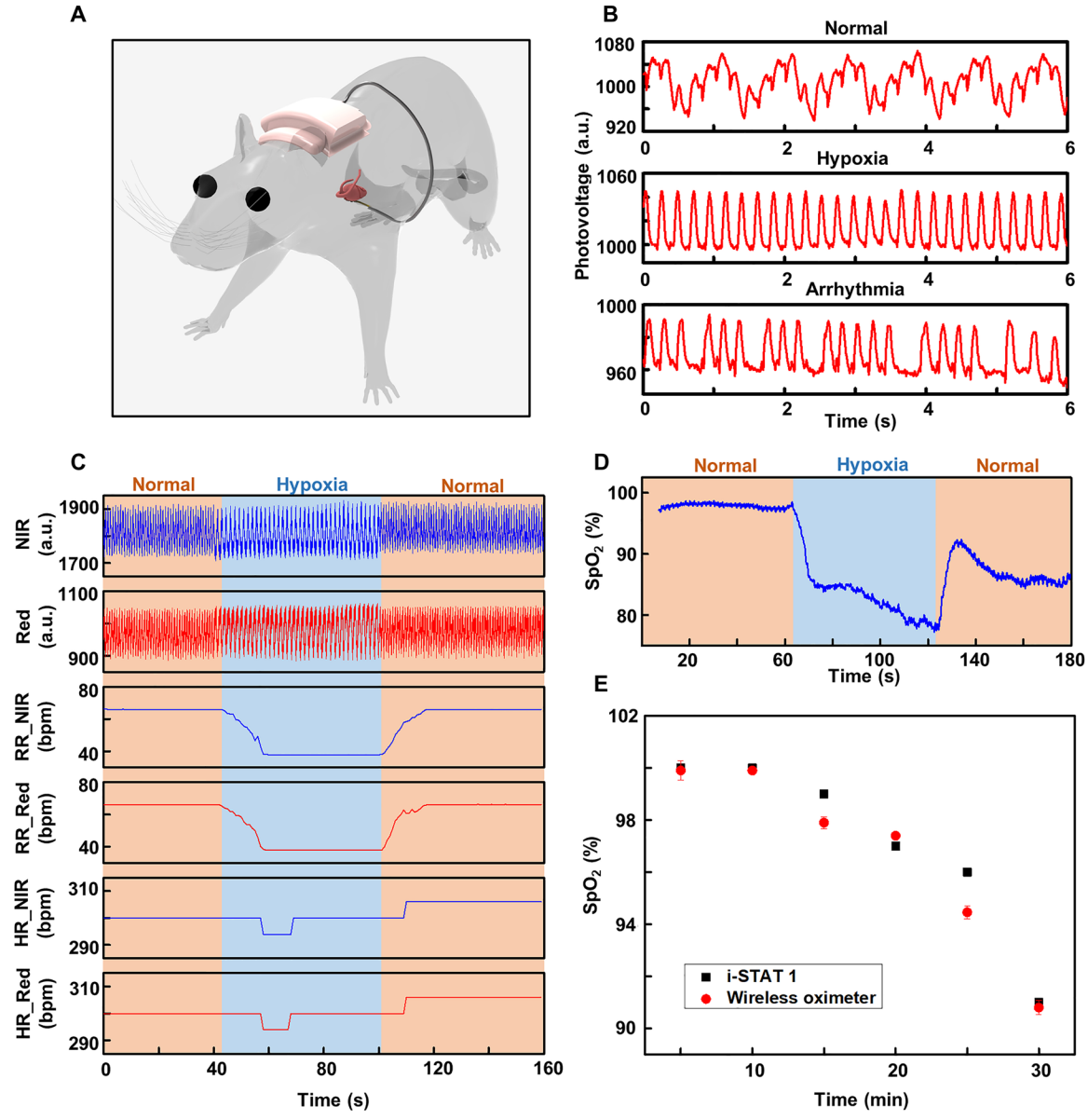

Fig. 5. In vivo demonstration of real-time monitoring of cardiac physiology in a rodent model. (**A**) 3D schematic illustration of the placement of the catheter oximeter around the heart of a rat with the wireless module placed on the back. (**B**) Signal waveform captured with this system. Modifying the settings associated with the ventilator that supports respiration provides access to different cardiac conditions (labeled as Normal, Hypoxia, and Arrhythmia). (**C**) Measurements of cardiac activity (beating patterns, HR, and RR). (**D**) Measured oxygenation of the heart. Induced changes in cardiac pulse oximetry (SpO_2) match well with the changes on the ventilator machine. (**E**) Measured cardiac oxygenation using the wireless catheter oximeter and using a commercial blood gas analyzer. The analyzer measures blood sampled from the left ventricle, while the wireless catheter oximeter measures the oxygen saturation from the heart surface immediately after collecting blood samples.

coronary artery. Adjustments of the ventilation rate and tidal volume on the ventilator allow induced hypoxia and arrhythmias, for purposes of testing. As shown in Fig. 5B, the device captures changes in HR, respiration rate (RR), ischemia, and arrhythmias (n = 6 biologically independent rats, signal labeled as Normal, Hypoxia, and Arrhythmia, respectively). Figure 5C highlights the signals associated with probing with red and NIR light, each of which shows expected waveforms, along with calculated RR and HR from these signals (n = 6 rats per group). The RR follows the ventilator machine settings, i.e., 66 bpm in the beginning, 38 bpm in the middle, and back to 66 bpm until the end, while the HR follows a normal value for rats. Figure 5D summarizes calculated cardiac pulse oxygenation levels that can be captured by the implanted wireless sensing system. Figure 5E presents results for cardiac oxygenation (n = 4 biologically independent rats) and comparisons against measurements performed with a commercial blood gas analyzer using samples of blood from the left ventricle, starting with the initial phases of the open-chest experiment. The high degree of correlation (Pearson correlation = 0.971) demonstrates that the device offers sufficient sensitivity and precision in real-time oxygenation monitoring for use during cardiac surgery and associated surgical recovery (details on the measurements and signal processing algorithm appear in Materials and Methods).

DISCUSSION

The results presented here include design features, feasibility testing, and validation data for an implantable optoelectronic system tailored for use in cardiovascular monitoring, specifically in the context of surgical operations. The designs yield devices that are mechanically compliant and water resistant. This millimeter-scale, wireless optoelectronic platform enables chronic, continuous, precision sensing of intravascular or intracardiac oxygen saturation, free from the entanglement by conventional catheter oximeters. The advancement in mechanical compliance and material softness, compared with fiber-optic catheter, suggests opportunities in mitigating the complications seen by old technology. Moreover, the lateral mode of illumination maximizes light-tissue coupling, allowing a range of implantation sites including blood vessel and cardiac tissue. Comparison test and validation studies on blood samples, on human fingertips, and on cardiac surfaces in live animal models indicate measurement performance comparable to that of clinical standard oximeters and with values that match those determined with a blood gas analyzer.

The values of cardiac oxygenation saturation detected using the platforms described here correlate with the oxygenation of left ventricular blood measured using a blood gas analyzer in experiments on anesthetized rats. The wall thickness of the left ventricle in rats is 1.5 to 2.8 mm (*42*, *43*). With a penetration depth of 4 to 5 mm in muscular tissues, light can pass through the entire transmural extent of left ventricular wall to detect the oxygen saturation of the blood inside. As mentioned previously, the penetration depth can be changed by adjusting the optical power. Future studies will examine the efficacy and reliability of the catheter-type oximeter in quantifying the oxygen saturation of the heart, superior vena cava, and main pulmonary artery in larger animals and patients undergoing open-heart surgery.

These in vivo results must, however, be interpreted within the constraints of a few potential limitations. In addition to intracardiac oxygen saturation, oxygenation levels of the superior vena cava or main pulmonary artery are important in open-heart surgery. The small-animal studies here prevent evaluations of capabilities in such anatomic locations. Additional work is necessary to test the accuracy and efficacy of the device in these major vascular locations acutely, and after the chest is closed in larger animals. The small-animal studies also prevent in vivo chronic demonstration of the reported device. Systematic examination of the inflammatory responses associated with subdermal implantation of the optical probes reveals no observable increases in leukocytes, indicating negligible inflammatory response (Fig. 3, G and H). Experiments to examine effects with large-animal models are a subject of ongoing work. Another research direction is to examine further, through in vivo experiments, the mechanical compliance of the presented catheter and associated capabilities for mitigating complications often encountered with conventional fiber-optic systems, such as blood vessel damage, infection, and thrombosis. Other possibilities for future work include incorporation of multiple LEDs and additional wavelengths for additional measurement capabilities and by integrating collections of PDs for depth profiling. Additional options are in combinations with sensors of pressure (*44*, *45*) and flow (*46*, *47*) or for drug delivery, using concepts adapted from those recently reported for animal experiments in neuroscience (*48*–*50*).

In conclusion, the present study indicates that a flexible, thin, catheter-type oximeter can accurately monitor venous and cardiac oxygenation levels in real time. Specifically, results demonstrate that this millimeter-scale, wireless optoelectronic platform can detect cardiac oxygenation saturation in rats during open-heart surgery. To explore the potential of the device to monitor oxygenation levels in main vessels, further studies will focus on the efficacy and reliability for detecting the oxygenation saturation in the superior vena cava and main pulmonary artery of large animals, mimicking open-heart surgery of patients.

MATERIALS AND METHODS

Fabrication of catheter-type oximeter probe

A flexible sheet of copper-clad polyimide (PI) (Cu/PI/Cu, 18/75/18 μm, AP8535R, Dupont, Pyralux) served as the substrate for the fPCB, with conductive traces, pads, and outline defined by patterned ablation of the copper using an ultraviolet (UV) laser system (ProtoLaser U4, LPKF Co.). The surface mount (SMT) electronic components, red, NIR LEDs, and PD were placed and attached using reflow soldering with low-temperature solder paste (Indalloy 290, Indium Corporation). This electronics module was connected to a detachable connector through four Teflon-coated copper wires (40 AWG enameled copper, Remington Industries) with a length between a few centimeters to 30 cm, depending on the application. Both the electronics module and the thin wires were inserted into a flexible tube (Tygon S3 E3630 Flexible Tubings, Fisher Scientific). A biocompatible silicone (MED-1000, Avantor Inc., mixed with 5% of Silc-Pig silicone opaque dye) prepolymer injected into the tube using a syringe was fully cured in 12 hours. The flexible tube was then removed.

Design and fabrication of the electronic modules

The wireless electronics module was designed using EAGLE 8.5 (Autodesk Inc.). The schematic and PCB layout are in the Supplementary Materials. A micropower, zero-input crossover distortion amplifier (ADA4505-1, Analog Devices Inc.) acts as a transimpedance amplifier. A BLE microcontroller (NRF52832, Nordic Semiconductor Inc.) with a custom program performs data sampling, controls the LEDs in low–duty cycle mode, executes data processing, and operates Bluetooth communication. With a feedback resistor of 2 megohms, the catheter probe and the wireless electronic module have a dark noise (root mean square) of 1.9 mV for NIR LED and 1.72 mV for red, which correspond to a photocurrent sensitivity of 0.95 nA for NIR LED and 0.86 nA for red.

Fabrication involved procedures similar to those described above, with an fPCB patterned using the laser ablation tool, and SMT components assembled using reflow soldering. A three-axis milling machine (Roland MDX-540) formed aluminum molds in geometries defined by three-dimensional (3D) computer-aided design (CAD) drawings created using ProE Creo 3.0. Films of a soft silicone material (Silbione RTV 4420, part A and part B, mixed with 5% of Silc-Pig silicone opaque dye) created in the mold by drop-casting and other films formed by spin-casting (250 rpm) on glass slides, both thermally cured in an oven (70°C for 30 min), served as top and bottom layers, respectively, for a soft, encapsulating enclosure. Placing the fully assembled electronic module into the molded layer, pouring a solution of soft silicone to fill the voids in between electronics and the top layer, and attaching the glass slides with silicone films defined the surface for the skin interface. Clamping the parts together and placing the entire assembly into an oven for curing (70°C for 30 min) completed the encapsulation. A final cutting process with a CO_2 laser

(Universal Laser Systems, Inc.) defined a smooth perimeter boundary for the system, and a manual cutting process with a small blade defined openings for the connector and switch.

Characterization of the optoelectronic performance

Spectroscopic measurements (using FOIS-1 Fiber Optic Integrating Sphere, Ocean Optics; FLAME-S-UV-VIS Spectrometer, Ocean Optics) yielded the emission spectra for the red and NIR LEDs. Exposing the photodetector to light passed through a chopper and recording the photocurrent using a data acquisition system (PXI-1031, National Instruments) provided measurements of the response time.

Monte Carlo simulation of the optical characteristics

Simulations of light transport in biological tissues used Monte Carlo methods for the devices reported here and for conventional fiber-optic systems to define the spatial illumination profiles (*31*). The simulations used a 3D computational space with 700 × 700 × 700 bins of 8×10^{-9} cm^3 volume and a total of 11×10^6 photon packets for each simulation. Commercial LEDs with peak emission wavelengths at 645 nm (red) and 950 nm (NIR) served as light sources, with both active illumination areas of 0.25 mm × 0.25 mm and emission angles of ±60°. For the optical fiber system, the optical core had a diameter of 0.2 mm and a numerical aperture of 0.22 to yield illumination in a ±9.5° emission cone in aqueous solution ($n_{aqueous}$ = 1.38). The irradiances at the illumination surfaces for both setups were 9.21 mW/mm^2 for red and 14.4 mW/mm^2 for NIR. Light propagation was simulated in cardiac muscle tissue with the corresponding wavelength-dependent scattering anisotropy factor ($g_{Red\text{-}m}$ = 0.93, $g_{NIR\text{-}m}$ = 0.93), absorption coefficient ($\mu_{a\text{-}Red\text{-}m}$ = 0.56 cm^{-1}, $\mu_{a\text{-}NIR\text{-}m}$ = 0.46 cm^{-1}), and scattering coefficient ($\mu_{s\text{-}Red\text{-}m}$ = 79 cm^{-1}, $\mu_{s\text{-}NIR\text{-}m}$ = 64 cm^{-1}) (*32*). Additional simulations in aqueous solution defined the illumination profiles produced by both systems at the red wavelength. The scattering anisotropy factor ($g_{Red\text{-}a}$ = 0.95), scattering coefficient ($\mu_{s\text{-}Red\text{-}a}$ = 1 cm^{-1}), and absorption coefficient ($\mu_{a\text{-}Red\text{-}a}$ = 0.43 cm^{-1}) were used for a solution with 1.6 μM concentration of fluorescent dye (Alexa Fluor 647) as a local illumination reporter (molecular weight = 1.25 kDa and $\varepsilon = 270 \times 10^3$ cm^{-1} M^{-1}). The illumination profile was extracted from the simulation volume given by the photon fluence (ϕ), which represents the phenomenological optical irradiance.

Figure 2C (right) presents results of simulations for the catheter probe in cardiac muscle tissue. Figure 2C (left), presented as a 3D rendering (Paraview 5.7.0), highlights the 0.01 mW/mm^2 fluence contour for red and NIR illumination (*51*). Figure S4A shows the light decay from the catheter–muscle tissue interface along the LED's normal direction. Furthermore, fig. S4B shows the illumination volume in muscle tissue predicted by the simulations at different irradiance thresholds. For an illumination threshold of 0.01 mW/mm^2, the penetration depth from the catheter-muscle interface along the LED's normal direction is 3.84 and 5.16 mm, and the illumination volume of the tissue is 85.3 and 159.8 mm^3 for the red and NIR wavelengths, respectively. Figure 4A (right) shows the simulated illumination profiles, produced by red light for the catheter-type probe and the optical fiber in aqueous solution.

Characterization of the thermal properties of the catheter oximeter probe

An NTC component (ERTJZEG103FA, with dimensions of 600 μm × 300 μm × 300 μm, Panasonic Co.) attached to the outer encapsulation layer, at a position directly above the LEDs, yielded measurements of temperature for the case of insertion inside a piece of pork belly. The thermistor was connected to the input of a digital multimeter (PXIE-4065, National Instruments) through Teflon-coated copper wires (40 AWG enameled copper, Remington Industries) for continuous resistance measurements. The oximeter probe was activated at 1 min and deactivated at 4 min, for a total recording of 6 min. Converting the resistances into temperatures using the manufacturer's specifications yielded changes in temperature as a function of time during this simple on-and-off cycle, as shown in Fig. 2E.

Heat transfer analysis (fig. S5) was performed with the commercial software COMSOL 5.2a (Heat Transfer Model User's Guide) to compute the change in temperature (ΔT) in the heart as a result of the thermal power associated with operation of the LEDs and with absorption of the emitted light. Heat generated by cardiac metabolism and the effects of blood perfusion were not considered in the simulation. The Pennes' bioheat equation (*52*) is then written as

$$\rho C_p \frac{\partial T}{\partial t} + \nabla \cdot (-k \ \nabla \ T) = Q_{the} + \phi \mu_a$$

where T is the temperature; t is the time; k, ρ, and C_p are the thermal conductivity, mass density, and heat capacity of the heart, respectively; and Q_{the} is the heat generated from thermal power of the LEDs. The heat associated with light emission was calculated as the product of the light fluence rate ϕ obtained in the optical simulation and the absorption coefficient μ_a of the cardiac muscle tissue. The optical and thermal properties appear in Tables 1 and 2. The cardiac tissue, probe geometry, and the LEDs were modeled using four-node tetrahedral elements. Convergence tests of the mesh size were performed to ensure accuracy. The total number of elements in the models was approximately 650,000.

Measurements of Young's moduli

The Young's moduli of different coating materials were measured by indentation testing (Hysitron BioSoft Indenter, Bruker) with an indenter radius of r = 200 μm. Tests on films of different materials (~1 mm in thickness) generated force-displacement curves upon contact of the indenter and the film surface. The Young's modulus was calculated by fitting the force-displacement data within an indentation depth δ = 20 μm using a Hertzian contact model.

Measurements of bending stiffness

Catheter tubes with different coating materials and conductive copper wire diameters exhibit different bending stiffnesses, as measured by cantilever bending tests using a dynamic mechanical analyzer (RSA-G2, TA Instruments). A wire sample (L = 19 mm) with one end clamped and the other end under a point load applied by an indenter served as a cantilever for bending stiffness measurement (fig. S7A). For a cantilever beam with a point load at the end, under small deflections,

Table 1. Cardiac muscle tissue absorption coefficients μ_a (cm^{-1}) used in the optical simulations at red and NIR wavelengths.

	Red light (645 nm)	NIR light (950 nm)
Cardiac tissue	0.56	0.46

Table 2. Thermal properties of materials and cardiac tissues used in the thermal simulations.

	Thermal conductivity k ($W\,m^{-1}\,K^{-1}$)	Specific heat capacity C_p ($J\,kg^{-1}\,K^{-1}$)	Density ρ ($kg\,m^{-3}$)
Cardiac	0.493	3212	1041
Copper	377	385	8960
Polyimide	0.21	2100	909
PDMS	0.2	1460	970
LEDs	130	490	6100

the relationship among the end deflection δ, force F, and bending stiffness EI is given by

$$\delta = \frac{FL^3}{3EI}, \text{for } \delta \ll L$$

The bending stiffness EI can then be calculated as

$$EI = \frac{FL^3}{3\delta}$$

For each measurement, the force-displacement data from initial contact between the indenter and the wire to a deflection of δ = 0.2 mm were used for the calculation of bending stiffness. Four measurements at different sections of the wire were taken for each sample.

Characterization of the mechanical properties of the catheter oximeter probe

The FEA commercial software ABAQUS (Analysis User's Manual 2010, v6.10) was used to study the mechanics and to optimize the design layouts and materials selections. The objective was to decrease the strains in the Cu wire interconnects and the Cu layers in the sensor probe during mechanical deformations. The silicone, Cu wires (80 μm diameter), and PI films (75 μm thick) were modeled by hexahedron elements (C3D8R), while the thin Cu layer (18 μm thick) of the fPCB was modeled by shell elements (S4R). The minimal element size was one-fifth of the width of the narrowest interconnects (15 μm) to ensure the convergence of the mesh and the accuracy of the simulation results. The values of the elastic modulus (E) and Poisson's ratio (ν) used in the analysis were E_{Cu} = 119 GPa, ν_{Cu} = 0.34, E_{PI} = 2.5 GPa, ν_{PI} = 0.34, $E_{Slicone}$ = 1 MPa, and $\nu_{Slicone}$ = 0.49.

Cyclic bending and PBS soaking tests

The two ends of a device were clamped (the distance between the two clamped ends is 4 cm) to two translational stages. Repeatedly moving one translational stage toward the other back and forth by a distance of 3 cm led to bending of the probe to minimum bending radius of ~5 mm. After every 2000 bending cycles, the probe was removed from the apparatus, inserted into an integrating sphere (Fiber Optic Spectrometer FOIS-1 Integrating Sphere, Ocean Optics), connected to the electronic module, and activated to yield measurements of photovoltages corresponding to emission from the two LEDs. Gripping the tip of the probe between the thumb and index finger, connecting the probe to the electronic module, and operating the system yielded photoplethysmograms. Such tests were performed up to 10,000 bending cycles. The soak tests began with immersion of the probe into a chamber filled with PBS and mounting in an oven at 37°C. Evaluations of the devices occurred once per week, according to procedures described above, for a total of 8 weeks.

In vivo tests of biocompatibility

A medical-grade autoclave system (Tuttnauer EZ10 Fully Automatic Autoclave) was used to sterilize the optical sensing probe, with LEDs, PD, and light-blocking elements on the fPCB, and fully encapsulated with a medical-grade silicone material (MED-1000) in a cylinder (diameter, 1.5 mm; length, 16 mm) just before implantation. The procedures involved anesthetizing a female CD-1 mouse (Charles River Laboratories) with isoflurane gas (~2%), opening a 2-cm-length pocket at the subcutaneous region on the back near the spine, inserting the device into the pocket, and suturing to close the surgical opening. The procedures were approved by the Institutional Animal Care and Use Committee of Northwestern University (protocol IS00005877). The health status of each animal was checked daily. Euthanizing the mice at 1 month after device implantation preceded the extraction of blood. Charles River Laboratories conducted complete blood counts and blood chemistry tests on samples collected in K-EDTA tubes and gel tubes, respectively.

Analysis of complete blood count (Fig. 3G) and blood chemistry (Fig. 3H) for mice with the probe implanted in subcutaneous region on the back near the spine for 30 days (labeled as Experiment) and for mice without device implantation (labeled as Control) indicated no sign of organ damage or injury and no change in the electrolyte and enzyme balance for 1 month. During the period of study, the data showed no notable change in average count of white blood cells (WBC), red blood cells (RBC), platelets (PLT), hemoglobin (HGB), hematocrit (HCT), mean corpuscular volume (MCV), mean corpuscular hemoglobin (MCH), red cell distribution width (RDW), and mean platelet volume (MPV) compared with control group, indicating the absence of any abnormalities, including anemia, nutritional deficiency, liver disease, bleeding disorder, and heart attack (Fig. 3G and fig. S13A). Tests of blood chemistry yielded information on enzymes and electrolytes, as diagnostic biomarkers of organ-specific diseases and metabolic disorders. In all cases, the results fell within confidence intervals of control values (Fig. 3H and fig. S13B). Specifically, normal levels of albumin (ALB), total protein (TP), alanine aminotransferase (ALT), alkaline phosphatase (ALP), and aspartate transaminase (AST) indicated normal liver function. Normal levels of blood urea nitrogen (BUN) and creatine (CREA) indicated normal kidney function. Normal levels of glucose (GLU), calcium (Ca), sodium (Na), potassium (K), chloride (Cl), and phosphorus (PHOS) suggested normal function of the metabolic system.

In vitro experiments to compare the performance of the wireless catheter oximeter with a conventional fiber-optic device

Defibrinated horse blood (100 ml, from Fisher Scientific) contained in a cylindrical reservoir (diameter, 4 cm; height, 30 cm) was maintained at 37.0 ± 0.1°C with a temperature controller (Fisher Scientific). Inserting both the catheter probe of the wireless sensing system and a commercial fiber-optic catheter oximeter (Swan Ganz 777F8, recorded by HemoSphere monitoring platform, Edwards LifeSciences Inc.) into the reservoir with the sensing tips 3 cm below the surface of the horse blood and in the center of the reservoir to eliminate effects of the reservoir sidewalls enabled comparative measurements

of oxygenation. Adding reducing agents (ranging from 0.01 to 0.1 mg of sodium dithionite, purchased from MilliporeSigma) into the reservoir converted some of the oxygenated hemoglobin into deoxygenated hemoglobin, to define, in a controlled manner, the oxygenation level across a relevant range from 35 to 73%.

Human tests of pulse oximetry

Testing on human subjects involved placing the wireless catheter probe on the index figure. A standard transmissive oximeter (GE DASH 3000) was clasped on the index finger of the other hand (fig. S15). Both systems recorded HR and oximetry information from subjects simultaneously for roughly 4 min (Fig. 4, F and G, and fig. S17). In the experiment, the subject remained at rest for the first 30 s to define a baseline and then began to breath hold, followed by normal breathing until the end of experiment. A diverse group of subjects ($N > 4$, including East Asian, Indian, and Caucasian) demonstrated the device capabilities across a range of physical conditions and skin types.

In vivo experiments to measure cardiac physiology

Male Sprague-Dawley rats (weight, 400 to 500 g; age, 14 to 16 weeks) were purchased from Charles River Laboratories (Wilmington, MA). The animals were kept on a 12-hour light-dark cycle in a temperature-controlled room. The experimental procedures were approved by the Animal Care and Use Committee of the Northwestern University and conformed to the *Guide for the Care and Use of Laboratory Animals* (Institute for Laboratory Animal Research, National Academy of Sciences, ed. 8, 2011).

Sprague-Dawley rats were initially anesthetized in a chamber with isoflurane gas (5% isoflurane and 100% oxygen). Once consciousness was lost, the animals were intubated with a 16-gauge flexible catheter, and endotracheal tube was connected to a mechanical ventilator (Braintree VentStar ventilator) that provided positive-pressure ventilation with oxygen/isoflurane. The ventilator was set based on animal weight: tidal volume (Vt, milliliters) = $6.2 \times M^{1.01}$ and RR (min^{-1}) = $53.5 \times M^{-0.26}$, M = animal weight in kilograms. Each rat was connected to a vaporizer that delivers approximately 2.0% isoflurane driven by 100% oxygen. Rats were placed in the dorsal decubitus position on a warming platform. Intradermal bupivicaine was infiltrated at the incision sites approximately 10 min before incisions. Rats were maintained at approximately 37°C on a heating pad, with body temperature monitored throughout the experiment using a rectal temperature probe. The animal's hair was removed from the surgical site with hair removal cream NAIR after shaving. The surgical areas were scrubbed and disinfected with a povidone iodine prep pad, and the area was then wiped with an alcohol prep pad. Peripheral blood oxygen saturation was monitored throughout the experiment using a commercial pulse oximetry system (MouseSTAT Jr., Kent Scientific Co.).

Details of thoracotomy in rats appear elsewhere (*53*, *54*). Briefly, isoflurane-anesthetized rats were ventilated with room air supplemented with 100% oxygen. A left thoracotomy was performed at the fourth intercostal space, and the heart was suspended in a pericardial cradle. The left lung was gently pushed away from the pericardium with a small sponge. The oximeter probe was sutured to the anterior wall of the left ventricle close to the left anterior descending coronary artery with a nylon 6-0 suture, avoiding injuring coronary vessels. The oximeter wire went through a subcutaneous tunnel to the head. After instrumentation was completed, all rats were stabilized for 30 min and subjected to hypoxia by adjusting ventilation rate and tidal volume of the ventilator. The blood was withdrawn from the chamber of the left ventricle using a 27-gauge needle with a 1.0-ml syringe (shown in fig. S19). The blood samples were used to measure pH, SO_2, PO_2 (partial pressure of oxygen), and PCO_2 (partial pressure of CO_2) with a blood gas analyzer (i-STAT 1, Abaxis Inc.).

Data analysis and calculation of SpO_2

Analysis of pulse oximeter data relied on a commercial software package (MATLAB R2016b, The MathWorks Inc.). Data acquired from the two LEDs (red, 640 nm; IR, 950 nm) were provided by the system at a sampling frequency of 100 Hz. The signal at each wavelength was band-pass–filtered (0.5 to 3 Hz for human data, 3.5 to 6 Hz for animal data, fourth order, zero-lag Butterworth digital filter) to extract the main frequency of the pulsating component [AC(t)] and low-pass–filtered (0.5 Hz, fourth order, zero-lag Butterworth digital filter) to estimate the slow fluctuating signal unrelated to pulsation [DC(t), e.g., induced by respiration]. The relative pulsatile signal intensity $S(t)$ was computed as the ratio of the two signals for both the red and IR wavelengths

$$S(t) = \frac{\mathrm{AC}(t)}{\mathrm{DC}(t)} \tag{1}$$

A local minima (m) and maxima (M) identification algorithm in the signal $S(t)$ identified the peaks of each pulse cycle and yielded an interpolated modulation amplitude [$A(t)$] as

$$A(t) = M(t) - m(t) \tag{2}$$

The ratio $R(t)$ between the red and IR pulsatile components at every sample was evaluated in a moving integration window of 5 s as

$$R(t) = \sum_{5\,\mathrm{s}} \frac{\ln(A(t)_{\mathrm{R}} + 1)}{\ln(A(t)_{\mathrm{IR}} + 1)} \tag{3}$$

From photon-diffusion theory and the modified Lambert-Beer equation (*55*), the following equation can be derived to express the relationship between the percentage of arterial blood saturation [SpO_2(t)] and the $R(t)$

$$\mathrm{SpO_2(t)} = \frac{\varepsilon_{\mathrm{Hb_R}}\,\mathrm{DPF_{R/IR}} - \varepsilon_{\mathrm{Hb_{IR}}}\mathrm{R(t)}}{(\varepsilon_{\mathrm{Hb_R}} - \varepsilon_{\mathrm{HbO_{2R}}})\,\mathrm{DPF_{R/IR}} + (\varepsilon_{\mathrm{HbO_{2IR}}} - \varepsilon_{\mathrm{Hb_{IR}}})\,\mathrm{R(t)}} \cdot 100 \tag{4}$$

where $\varepsilon_{\mathrm{HbO_{2R}}}$ and $\varepsilon_{\mathrm{Hb_R}}$ are the extinction coefficients of HbO_2 and Hb for the red light, $\varepsilon_{\mathrm{HbO_{2IR}}}$ and $\varepsilon_{\mathrm{Hb_{IR}}}$ are the extinction coefficients of HbO_2 and Hb for the IR light, and $\mathrm{DPF_{R/IR}}$ describes the ratio between the differential pathlength factors (DPFs) at the two wavelengths of interest. The extinction coefficients of the two forms of hemoglobin at the wavelengths of interest were extracted from Zijlstra and colleagues (*56*): $\varepsilon_{\mathrm{HbO_{2R}}} = 0.011\ \mathrm{mm^{-1}}$, $\varepsilon_{\mathrm{Hb_R}} = 0.106\ \mathrm{mm^{-1}}$, $\varepsilon_{\mathrm{HbO_{2IR}}} = 0.028\ \mathrm{mm^{-1}}$, and $\varepsilon_{\mathrm{Hb_{IR}}} = 0.018\ \mathrm{mm^{-1}}$. The quantity $\mathrm{DPF_{R/IR}}$ describes the effects of the dissimilar optical path lengths (*57*). The color dependence of the optical path length depends on the scattering nature of the biological tissue and its dependence on the light wavelength. A practical problem when using Eq. 4 for SpO_2 estimation is that the DPF ratio depends on the baseline optical properties of the tissue, including the tissue microstructure and the SpO_2 itself (*58*). This issue can be addressed by calibrating the oximeter empirically. A constant DPF ratio can be considered over narrow ranges of saturation (80 to 100%). On the basis of literature and empirical results from our measurements, we set $\mathrm{DPF_{R/IR}} = 1.4$ (*58*, *59*). This

value accounted for the increased optical path length of red light compared to IR light. Equation 4 yields arterial oxygen saturation levels close to those determined by the commercial system on several subjects and across the full range of saturation levels investigated. The data were also used to determine the beats per minute, BPM(t). The time dependence of the BPM was estimated from the interbeat frequency $f(t)$, evaluated as the inverse of the difference between the times of two consecutive maxima $M(t)$ in the NIR, within an integration period of 5 s as

$$\mathrm{BPM}(t) = 60 f(t)_{\mathrm{IR,5\ s}} \tag{5}$$

Calculation of blood oxygen saturation

Evaluation of blood saturation in in vitro experiments used averages of red and IR values converted into optical densities (ODs) according to the equation

$$\mathrm{OD(i)} = -\ln(\mathrm{I(i)}/\mathrm{I_o}) \tag{6}$$

where I(i) is the recorded signal intensity in each experimental phase and I_o is its value in the first phase. In the absence of pulsating signals, assumptions on the baseline hemoglobin concentration and its oxygen saturation are required to infer changes in the saturation. We assumed a concentration of 15 g/dl for hemoglobin in the blood solution (*19*, *60*) and, based on the commercial catheter oximeter, an oxygen saturation of 39% in the first experimental phase. When considering that the molar mass of hemoglobin is 65 kg/mol, these assumptions yielded a baseline HbO_2 and Hb concentration in blood of HbO_{20} = 0.90 mM and Hb_0 = 1.41 mM, respectively. Calculation of changes in HbO_2, ΔHbO_2, and Hb, ΔHb, were evaluated using the modified Lambert-Beer law (*55*)

$$\begin{bmatrix}\Delta \mathrm{HbO_2(i)} \\ \Delta \mathrm{Hb(i)}\end{bmatrix} = \frac{1}{\rho_{\mathrm{eff}}}\begin{bmatrix}\varepsilon_{\mathrm{HbO_{2R}}} & \varepsilon_{\mathrm{Hb_R}} \\ \varepsilon_{\mathrm{HbO_{2IR}}} & \varepsilon_{\mathrm{Hb_{IR}}}\end{bmatrix}^{-1} \mathrm{X}\begin{bmatrix}\mathrm{OD_R(i)} \\ \mathrm{OD_{IR}(i)}\end{bmatrix} \tag{7}$$

where ρ_{eff} is the effective photon path in the back-reflection recording geometry and ε are the extinction coefficients for the two chromophores.

The saturation of blood for each phase was estimated as

$$\mathrm{SO_2(i)} = \frac{\mathrm{HbO_{20}} + \Delta \mathrm{HbO_2(i)}}{\mathrm{HbO_{20}} + \Delta \mathrm{HbO_2(i)} + \mathrm{Hb_0} + \Delta \mathrm{Hb(i)}}$$

The effective photon path of the probe was estimated experimentally by fitting SO_2(i) to the commercial catheter oximeter saturation values, as shown in fig. S15.

SUPPLEMENTARY MATERIALS

Supplementary material for this article is available at http://advances.sciencemag.org/cgi/content/full/7/7/eabe0579/DC1

View/request a protocol for this paper from *Bio-protocol*.

REFERENCES AND NOTES

1. F. Bloos, K. Reinhart, Venous oximetry. *Intensive Care Med.* **31**, 911–913 (2005).
2. J. Frazier, Theory and clinical application of continuous fiberoptic central venous oximetry (scvo2) monitoring. Critical Care Marketing and Education (Edwards Lifesciences, 2009).
3. J. Kim, P. Gutruf, A. M. Chiarelli, S. Y. Heo, K. Cho, Z. Xie, A. Banks, S. Han, K. I. Jang, J. W. Lee, K. T. Lee, X. Feng, Y. Huang, M. Fabiani, G. Gratton, U. Paik, J. A. Rogers, Miniaturized battery-free wireless systems for wearable pulse oximetry. *Adv. Funct. Mater.* **27**, 1604373 (2017).
4. M. Nitzan, A. Romem, R. Koppel, Pulse oximetry: Fundamentals and technology update. *Med. Devices* **7**, 231–239 (2014).
5. D. P. Guensch, K. Fischer, C. Jung, S. Hurni, B. M. Winkler, B. Jung, A. P. Vogt, B. Eberle, Relationship between myocardial oxygenation and blood pressure: Experimental validation using oxygenation-sensitive cardiovascular magnetic resonance. *PLOS ONE* **14**, e0210098 (2019).
6. J. L. Waller, J. A. Kaplan, D. I. Bauman, J. M. Craver, Clinical evaluation of a new fiberoptic catheter oximeter during cardiac surgery. *Anesth. Analg.* **61**, 676–679 (1982).
7. O. J. Liakopoulos, J. K. Ho, A. Yezbick, E. Sanchez, C. Naddell, G. D. Buckberg, R. Crowley, A. Mahajan, An experimental and clinical evaluation of a novel central venous catheter with integrated oximetry for pediatric patients undergoing cardiac surgery. *Anesth. Analg.* **105**, 1598–1604 (2007).
8. G. Marx, K. Reinhart, Venous oximetry. *Curr. Opin. Crit. Care* **12**, 263–268 (2006).
9. R. Pearse, A. Rhodes, Mixed and central venous oxygen saturation, in *Yearbook of Intensive Care and Emergency Medicine 2005* (Springer, 2005), pp. 592–602.
10. M. L. Landsman, N. Knop, G. Kwant, G. Mook, W. Zijlstra, A fiberoptic reflection oximeter. *Pflugers Arch.* **373**, 273–282 (1978).
11. S. D. Goldring, Google Patents (1987).
12. B. Boville, L. Young, Quick Guide to Pediatric Cardiopulmonary Care (Irvine: Edwards Lifesciences, 2015), pp. 3–78.
13. D. C. McGee, M. K. Gould, Preventing complications of central venous catheterization. *N. Engl. J. Med.* **348**, 1123–1133 (2003).
14. E. M. Kagel, G. M. Rayan, Intravenous catheter complications in the hand and forearm. *J. Trauma Acute Care Surg.* **56**, 123–127 (2004).
15. A. Bowdle, Vascular complications of central venous catheter placement: Evidence-based methods for prevention and treatment. *J. Cardiothorac. Vasc. Anesth.* **28**, 358–368 (2014).
16. H. S. Vats, Complications of catheters: Tunneled and nontunneled. *Adv. Chronic Kidney Dis.* **19**, 188–194 (2012).
17. C. Kornbau, K. C. Lee, G. D. Hughes, M. S. Firstenberg, Central line complications. *Int. J. Crit. Illn. Inj. Sci.* **5**, 170–178 (2015).
18. W. Bai, H. Yang, Y. Ma, H. Chen, J. Shin, Y. Liu, Q. Yang, I. Kandela, Z. Liu, S. K. Kang, C. Wei, C. R. Haney, A. Brikha, X. Ge, X. Feng, P. V. Braun, Y. Huang, W. Zhou, J. A. Rogers, Flexible transient optical waveguides and surface-wave biosensors constructed from monocrystalline silicon. *Adv. Mater.* **30**, e1801584 (2018).
19. W. Bai, J. Shin, R. Fu, I. Kandela, D. Lu, X. Ni, Y. Park, Z. Liu, T. Hang, D. Wu, Y. Liu, C. R. Haney, I. Stepien, Q. Yang, J. Zhao, K. R. Nandoliya, H. Zhang, X. Sheng, L. Yin, K. M. Renaris, A. Brikha, F. Aird, M. Pezhouh, J. Hornick, W. Zhou, J. A. Rogers, Bioresorbable photonic devices for the spectroscopic characterization of physiological status and neural activity. *Nat. Biomed. Eng.* **3**, 644–654 (2019).
20. H. U. Chung, B. H. Kim, J. Y. Lee, J. Lee, Z. Xie, E. M. Ibler, K. Lee, A. Banks, J. Y. Jeong, J. Kim, C. Ogle, D. Grande, Y. Yu, H. Jang, P. Assem, D. Ryu, J. W. Kwak, M. Namkoong, J. B. Park, Y. Lee, D. H. Kim, A. Ryu, J. Jeong, K. You, B. Ji, Z. Liu, Q. Huo, X. Feng, Y. Deng, Y. Xu, K. I. Jang, J. Kim, Y. Zhang, R. Ghaffari, C. M. Rand, M. Schau, A. Hamvas, D. E. Weese-Mayer, Y. Huang, S. M. Lee, C. H. Lee, N. R. Shanbhag, A. S. Paller, S. Xu, J. A. Rogers, Binodal, wireless epidermal electronic systems with in-sensor analytics for neonatal intensive care. *Science* **363**, eaau0780 (2019).
21. K. Lee, X. Ni, J. Y. Lee, H. Arafa, D. J. Pe, S. Xu, R. Avila, M. Irie, J. H. Lee, R. L. Easterlin, D. H. Kim, H. U. Chung, O. O. Olabisi, S. Getaneh, E. Chung, M. Hill, J. Bell, H. Jang, C. Liu, J. B. Park, J. Kim, S. B. Kim, S. Mehta, M. Pharr, A. Tzavelis, J. T. Reeder, I. Huang, Y. Deng, Z. Xie, C. R. Davies, Y. Huang, J. A. Rogers, Mechano-acoustic sensing of physiological processes and body motions via a soft wireless device placed at the suprasternal notch. *Nat. Biomed. Eng.* **4**, 148–158 (2020).
22. S. Y. Heo, J. Kim, P. Gutruf, A. Banks, P. Wei, R. Pielak, G. Balooch, Y. Shi, H. Araki, D. Rollo, C. Gaede, M. Patel, J. W. Kwak, A. E. Pena-Alcantara, K. T. Lee, Y. Yun, J. K. Robinson, S. Xu, J. A. Rogers, Wireless, battery-free, flexible, miniaturized dosimeters monitor exposure to solar radiation and to light for phototherapy. *Sci. Transl. Med.* **10**, eaau1643 (2018).
23. X. Yu, Z. Xie, Z. Xie, Y. Yu, J. Lee, A. Vazquez-Guardado, H. Luan, J. Ruban, X. Ning, A. Akhtar, D. Li, B. Ji, Y. Liu, R. Sun, J. Cao, Q. Huo, Y. Zhong, C. M. Lee, S. Y. Kim, P. Gutruf, C. Zhang, Y. Xue, Q. Guo, A. Chempakasseril, P. Tian, W. Lu, J. Y. Jeong, Y. J. Yu, J. Cornman, C. S. Tan, B. H. Kim, K. H. Lee, X. Feng, Y. Huang, J. A. Rogers, Skin-integrated wireless haptic interfaces for virtual and augmented reality. *Nature* **575**, 473–479 (2019).
24. K. Kwon, S. Y. Heo, I. Yoo, A. Banks, M. Chan, J. Y. Lee, J. B. Park, J. Kim, J. A. Rogers, Miniaturized, light-adaptive, wireless dosimeters autonomously monitor exposure to electromagnetic radiation. *Sci. Adv.* **5**, eaay2462 (2019).
25. H. Zhang, P. Gutruf, K. Meacham, M. C. Montana, X. Zhao, A. M. Chiarelli, A. Vázquez-Guardado, A. Norris, L. Lu, Q. Guo, C. Xu, Y. Wu, H. Zhao, X. Ning, W. Bai, I. Kandela, C. R. Haney, D. Chanda, R. W. Gereau IV, J. A. Rogers, Wireless, battery-free optoelectronic systems as subdermal implants for local tissue oximetry. *Sci. Adv.* **5**, eaaw0873 (2019).
26. Y. Mendelson, B. D. Ochs, Noninvasive pulse oximetry utilizing skin reflectance photoplethysmography. *IEEE Trans. Biomed. Eng.* **35**, 798–805 (1988).

27. J. L. Reuss, Multilayer modeling of reflectance pulse oximetry. *IEEE Trans. Biomed. Eng.* **52**, 153–159 (2005).
28. E. D. Chan, M. M. Chan, M. M. Chan, Pulse oximetry: Understanding its basic principles facilitates appreciation of its limitations. *Respir. Med.* **107**, 789–799 (2013).
29. P. Scott, Optical absorption of hemoglobin. *Oregon Medical Laser Center*. http://omlc.ogi.edu/spectra/hemoglobin (1999).
30. TEMD7000X01 datasheet; www.vishay.com, Rev. 1.6 (February 2015).
31. L. Wang, S. L. Jacques, *Monte Carlo Modeling of Light Transport in Multi-Layered Tissues in Standard C* (The University of Texas, MD Anderson Cancer Center, 1992), pp. 4–11.
32. A. N. Bashkatov, E. A. Genina, V. V. Tuchin, Optical properties of skin, subcutaneous, and muscle tissues: A review. *J. Innov. Opt. Health Sci.* **4**, 9–38 (2011).
33. A. Bouchama, J. P. Knochel, Heat stroke. *N. Engl. J. Med.* **346**, 1978–1988 (2002).
34. C. G. Crandall, T. E. Wilson, Human cardiovascular responses to passive heat stress. *Compr. Physiol.* **5**, 17–43 (2015).
35. P. G. Agache, C. Monneur, J. L. Leveque, J. De Rigal, Mechanical properties and Young's modulus of human skin in vivo. *Arch. Dermatol. Res.* **269**, 221–232 (1980).
36. A. Kalra, A. Lowe, A. A. Jumaily, An overview of factors affecting the skins Youngs modulus. *J. Aging Sci.* **4**, 2 (2016).
37. A. B. Mathur, A. M. Collinsworth, W. M. Reichert, W. E. Kraus, G. A. Truskey, Endothelial, cardiac muscle and skeletal muscle exhibit different viscous and elastic properties as determined by atomic force microscopy. *J. Biomech.* **34**, 1545–1553 (2001).
38. S. Y. Ho, Anatomy and myoarchitecture of the left ventricular wall in normal and in disease. *Eur. J. Echocardiogr.* **10**, iii3–iii7 (2009).
39. P. Ingelmo, M. Barone, R. Fumagalli, Importance of monitoring in high risk surgical patients. *Minerva Anestesiol.* **68**, 226–230 (2002).
40. K. Reinhart, H.-J. Kuhn, C. Hartog, D. L. Bredle, Continuous central venous and pulmonary artery oxygen saturation monitoring in the critically ill. *Intensive Care Med.* **30**, 1572–1578 (2004).
41. R. M. McAdams, R. J. McPherson, N. M. Dabestani, C. A. Gleason, S. E. Juul, Left ventricular hypertrophy is prevalent in Sprague–Dawley rats. *Comp. Med.* **60**, 357–363 (2010).
42. S. E. Litwin, S. E. Katz, J. P. Morgan, P. S. Douglas, Serial echocardiographic assessment of left ventricular geometry and function after large myocardial infarction in the rat. *Circulation* **89**, 345–354 (1994).
43. L. E. Watson, M. Sheth, R. F. Denyer, D. E. Dostal, Baseline echocardiographic values for adult male rats. *J. Am. Soc. Echocardiogr.* **17**, 161–167 (2004).
44. J. Shin, Y. Yan, W. Bai, Y. Xue, P. Gamble, L. Tian, I. Kandela, C. R. Haney, W. Spees, Y. Lee, M. Choi, J. Ko, H. Ryu, J. K. Chang, M. Pezhouh, S. K. Kang, S. M. Won, K. J. Yu, J. Zhao, Y. K. Lee, M. R. MacEwan, S. K. Song, Y. Huang, W. Z. Ray, J. A. Rogers, Bioresorbable pressure sensors protected with thermally grown silicon dioxide for the monitoring of chronic diseases and healing processes. *Nat. Biomed. Eng.* **3**, 37–46 (2019).
45. S. M. Won, H. Wang, B. H. Kim, K. Lee, H. Jang, K. Kwon, M. Han, K. E. Crawford, H. Li, Y. Lee, X. Yuan, S. B. Kim, Y. S. Oh, W. J. Jang, J. Y. Lee, S. Han, J. Kim, X. Wang, Z. Xie, Y. Zhang, Y. Huang, J. A. Rogers, Multimodal sensing with a three-dimensional piezoresistive structure. *ACS Nano* **13**, 10972–10979 (2019).
46. S. R. Krishnan, T. R. Ray, A. B. Ayer, Y. Ma, P. Gutruf, K. Lee, J. Y. Lee, C. Wei, X. Feng, B. Ng, Z. A. Abecassis, N. Murthy, I. Stankiewicz, J. Freudman, J. Stillman, N. Kim, G. Young, C. Goudeseune, J. Ciraldo, M. Tate, Y. Huang, M. Potts, J. A. Rogers, Epidermal electronics for noninvasive, wireless, quantitative assessment of ventricular shunt function in patients with hydrocephalus. *Sci. Transl. Med.* **10**, eaat8437 (2018).
47. R. C. Webb, Y. Ma, S. Krishnan, Y. Li, S. Yoon, X. Guo, X. Feng, Y. Shi, M. Seidel, N. H. Cho, J. Kurniawan, J. Ahad, N. Sheth, J. Kim, J. G. Taylor, T. Darlington, K. Chang, W. Huang, J. Ayers, A. Gruebele, R. M. Pielak, M. J. Slepian, Y. Huang, A. M. Gorbach, J. A. Rogers, Epidermal devices for noninvasive, precise, and continuous mapping of macrovascular and microvascular blood flow. *Sci. Adv.* **1**, e1500701 (2015).
48. Y. Zhang, D. C. Castro, Y. Han, Y. Wu, H. Guo, Z. Weng, Y. Xue, J. Ausra, X. Wang, R. Li, G. Wu, A. Vazquez-Guardado, Y. Xie, Z. Xie, D. Ostojich, D. Peng, R. Sun, B. Wang, Y. Yu, J. P. Leshock, S. Qu, C. J. Su, W. Shen, T. Hang, A. Banks, Y. Huang, J. Radulovic, P. Gutruf, M. R. Bruchas, J. A. Rogers, Battery-free, lightweight, injectable microsystem for in vivo wireless pharmacology and optogenetics. *Proc. Natl. Acad. Sci. U.S.A.* **116**, 21427–21437 (2019).
49. Y. Zhang, A. D. Mickle, P. Gutruf, L. A. McIlvried, H. Guo, Y. Wu, J. P. Golden, Y. Xue, J. G. Grajales-Reyes, X. Wang, S. Krishnan, Y. Xie, D. Peng, C. J. Su, F. Zhang, J. T. Reeder, S. K. Vogt, Y. Huang, J. A. Rogers, R. W. Gereau IV, Battery-free, fully implantable optofluidic cuff system for wireless optogenetic and pharmacological neuromodulation of peripheral nerves. *Sci. Adv.* **5**, eaaw5296 (2019).
50. J. W. Jeong, J. G. McCall, G. Shin, Y. Zhang, R. Al-Hasani, M. Kim, S. Li, J. Y. Sim, K. I. Jang, Y. Shi, D. Y. Hong, Y. Liu, G. P. Schmitz, L. Xia, Z. He, P. Gamble, W. Z. Ray, Y. Huang, M. R. Bruchas, J. A. Rogers, Wireless optofluidic systems for programmable in vivo pharmacology and optogenetics. *Cell* **162**, 662–674 (2015).
51. J. Ahrens, B. Geveci, C. Law, Paraview: An end-user tool for large data visualization, in *The Visualization Handbook* (Elsevier, 2005), vol. 717.
52. J. M. Stujenske, T. Spellman, J. A. Gordon, Modeling the spatiotemporal dynamics of light and heat propagation for in vivo optogenetics. *Cell Rep.* **12**, 525–534 (2015).
53. I. Baotic, D. Weihrauch, J. Procknow, J. Vasquez-Vivar, Z. D. Ge, S. Sudhakaran, D. C. Warltier, J. R. Kersten, Isoflurane favorably modulates guanosine triphosphate cyclohydrolase-1 and endothelial nitric oxide synthase during myocardial ischemia and reperfusion injury in rats. *Anesthesiology* **123**, 582–589 (2015).
54. Y. Liu, M. Paterson, S. L. Baumgardt, M. G. Irwin, Z. Xia, Z. J. Bosnjak, Z.-D. Ge, Vascular endothelial growth factor regulation of endothelial nitric oxide synthase phosphorylation is involved in isoflurane cardiac preconditioning. *Cardiovasc. Res.* **115**, 168–178 (2019).
55. A. Sassaroli, S. Fantini, Comment on the modified Beer-Lambert law for scattering media. *Phys. Med. Biol.* **49**, N255–N257 (2004).
56. W. G. Zijlstra, A. Buursma, W. P. Meeuwsen-van der Roest, Absorption spectra of human fetal and adult oxyhemoglobin, de-oxyhemoglobin, carboxyhemoglobin, and methemoglobin. *Clin. Chem.* **37**, 1633–1638 (1991).
57. F. Fabbri, A. Sassaroli, M. E. Henry, S. Fantini, Optical measurements of absorption changes in two-layered diffusive media. *Phys. Med. Biol.* **49**, 1183–1201 (2004).
58. J. L. Kohl, G. Noci, E. Antonucci, G. Tondello, M. C. E. Huber, S. R. Cranmer, L. Strachan, A. V. Panasyuk, L. D. Gardner, M. Romoli, S. Fineschi, D. Dobrzycka, J. C. Raymond, P. Nicolosi, O. H. W. Siegmund, D. Spadaro, C. Benna, A. Ciaravella, S. Giordano, S. R. Habbal, M. Karovska, X. Li, R. Martin, J. G. Michels, A. Modigliani, G. Naletto, R. H. O'Neal, C. Pernechele, G. Poletto, P. L. Smith, R. M. Suleiman, UVCS/SOHO empirical determinations of anisotropic velocity distributions in the solar corona. *Astrophys. J.* **501**, L127–L131 (1998).
59. F. Scholkmann, U. Gerber, M. Wolf, U. Wolf, End-tidal CO2: An important parameter for a correct interpretation in functional brain studies using speech tasks. *Neuroimage* **66**, 71–79 (2013).
60. Signs & Symptoms of Anemia in Horses; https://succeed-equine.com/ (2014).

Acknowledgments: We thank C. Haney for processing the microCT images, A. Kandela and I. Stepien for providing subdermal biocompatibility experiments, and A. Banks for providing commercial catheter system. **Funding:** This work was funded by the Center for Bio-Integrated Electronics at Northwestern University. H. Zhang acknowledges the support from the National Natural Science Foundation of China (grant no. 21974079). Z.X. acknowledges the support from the National Natural Science Foundation of China (grant no. 12072057) and Fundamental Research Funds for the Central Universities (grant no. DUT20RC(3)032). X.Y. acknowledges the support from the City University of Hong Kong (grant no. 9610423). Y.H. acknowledges support from NSF (CMMI1635443). R.A. acknowledges support from the National Science Foundation Graduate Research Fellowship (NSF grant number DGE-1842165) and the Ford Foundation Predoctoral Fellowship. We also acknowledge funding from the Querrey Simpson Institute for Bioelectronics. **Author contributions:** W.L., H. Zhang, J.F., and J.A.R. led the development of the concepts and designed the experiments. W.L., W.B., and H. Zhang led the experimental work with support from C.X., H.S., K.N., H. Zhao, K.L. Y.W., S.X., A.R., M.H., K.K., and E.B.T. A.V.-G. and D.F. performed the optical simulation. Z.X., R.A., Y.D., and Y.H. performed mechanical and thermal modeling and simulation. Z.-D.G. led the animal experiment with support from W.L. and W.B. A.M.C. and W.L. developed the algorithm and performed the oximetry data analysis. W.L. and J.A.R. led in writing the manuscript. All authors commented on the manuscript. **Competing interests:** The authors declare that they have no competing interests. **Data and materials availability:** The electronics design file, the program code, and software for operating the wireless catheter oximeter of this study are available from the corresponding author upon reasonable request. The data supporting the findings of this study are available from the corresponding author on reasonable request.

Submitted 30 July 2020
Accepted 23 December 2020
Published 10 February 2021
10.1126/sciadv.abe0579

Citation: W. Lu, W. Bai, H. Zhang, C. Xu, A. M. Chiarelli, A. Vázquez-Guardado, Z. Xie, H. Shen, K. Nandoliya, H. Zhao, K. Lee, Y. Wu, D. Franklin, R. Avila, S. Xu, A. Rwei, M. Han, K. Kwon, Y. Deng, X. Yu, E. B. Thorp, X. Feng, Y. Huang, J. Forbess, Z.-D. Ge, J. A. Rogers, Wireless, implantable catheter-type oximeter designed for cardiac oxygen saturation. *Sci. Adv.* **7**, eabe0579 (2021).